Available online at www.sciencedirect.com
ScienceDirect
Earth and Planetary Science Letters 249 (2006) 484–493
EPSL
www.elsevier.com/locate/epsl

Semi-brittle flow during dehydration of lizardite–chrysotile serpentinite deformed in torsion: Implications for the rheology of oceanic lithosphere

Takehiro Hirose [a,*,1], Misha Bystricky [a,b], Karsten Kunze [a], Holger Stünitz [c]

[a] Geologisches Institut, ETH Zentrum, Zurich, CH-8092, Switzerland
[b] LMTG, UMR 5563, Observatoire Midi-Pyrénées, Université Paul-Sabatier, 31400 Toulouse, France
[c] Department of Earth Sciences, Basel University, Basel, CH-4056, Switzerland

Received 2 October 2005; received in revised form 4 July 2006; accepted 12 July 2006
Available online 17 August 2006
Editor: R.D. van der Hilst

Abstract

Serpentinite is a significant component of the oceanic lithosphere and plays an important role in subduction dynamics. However, the rheology of serpentine-bearing rocks is poorly understood, especially at large strains and during the dehydration of serpentine. We have investigated the mechanical behavior and microstructural evolution of serpentinite during dehydration reaction to olivine, talc and water at temperatures of 550 and 600 °C, pressures of 300 and 400 MPa and shear strain rates of 1×10^{-5} to 1×10^{-4} s^{-1} under drained conditions. The non-coaxial deformation experiments were performed in a gas-medium apparatus equipped with a torsion system to shear strains of up to 3.3. Strong crystallographic preferred orientations (CPO) of partially dehydrated serpentine, shear localization through the development of S–C structures and widespread microfracturing in deformed specimens indicate that deformation took place in the semi-brittle field. Microstructural observations reveal that the CPO results from slip and rotation of (001) planes in partially dehydrated lizardite, possibly assisted by fluid released by the reaction. Despite the development of a strong CPO and shear localization, strain hardening accompanied by repeated transitory stress drops of a few MPa was observed and may be explained by the following combined effects: (1) progressive decrease of excess local pore pressures due to specimen dilatancy and the formation of pore networks during the reaction, leading to an increase in effective pressure, (2) subsequent collapse of this pore space by shear-enhanced compaction, resulting in work hardening, and (3) formation of a mechanically stronger assemblage of reaction products. The experiments imply that the bulk strength of a serpentinized subducting slab increases during dehydration as fluid escapes from the slab, while local embrittlement and shear localization take place.

Keywords: serpentinite; dehydration; crystallographic preferred orientation; strain hardening; semi-brittle flow

1. Introduction

Serpentinites form by extensive hydration of mantle rocks in the oceanic lithosphere. Dehydration of serpentine to olivine and hydrous phases during prograde metamorphism may play an important role in the localization of

* Corresponding author. Tel.: +81 75 753 4157; fax: +81 75 753 4189.
E-mail addresses: hirose@kueps.kyoto-u.ac.jp (T. Hirose), bystricky@lmtg.obs-mip.fr (M. Bystricky), kunze@erdw.ethz.ch (K. Kunze), holger.stuenitz@unibas.ch (H. Stünitz).
[1] Now at: Department of Geology and Mineralogy, Graduate School of Science, Kyoto University, Kyoto, 606-8502, Japan.

0012-821X/$ - see front matter © 2006 Elsevier B.V. All rights reserved.
doi:10.1016/j.epsl.2006.07.014

deformation into shear zones in the oceanic lithosphere [1,2] and in the occurrence of intermediate-depth earthquakes along subduction zones (e.g., [3–6]). Quantitative rheological and microstructural data from laboratory deformation experiments on serpentinites are necessary in order to gain a better understanding of these fundamental geological processes.

Previous deformation studies on serpentinites proposed dehydration embrittlement as a potential mechanism for intermediate-depth earthquakes [3,7]. In these studies, weakening and embrittlement of serpentinite was observed when the experiments were performed under undrained conditions (i.e., where fluid was not allowed to escape the sample assembly). Deformation of serpentinite under controlled pore fluid pressure led to the formation of shear zones of ultrafine-grained olivine deforming by diffusion-accommodated grain-boundary sliding [8,9]. The formation of these olivine-rich zones was accompanied by significant weakening at low strain rates, offering a possible explanation for the anomalous seismic properties of oceanic transform fault zones [9].

All of these experiments were performed at conditions (confining pressures up to 500 MPa) where local excess pore pressures develop, because the fluid volume produced during the dehydration reaction is greater than the pore space resulting from the formation of olivine and hydrous phases from serpentine. High pore pressures are inevitable in undrained specimens but may also develop under drained conditions since serpentinites have very low permeability [10]. By contrast, subducting slabs dehydrate at pressures (>2 GPa) where the total volume change during the reaction is negative and no excess pore pressure develops. Recently, dehydration embrittlement of serpentinite was also observed at these high pressures under undrained conditions [11]. However, as all experimental studies up to now were performed to low total shear strains, it was difficult to evaluate the effect of microstructural evolution during dehydration on the mechanical properties of serpentinite.

In this study we investigate how the mechanical behavior of serpentinite changes with strain during dehydration by performing deformation experiments to large shear strains under drained conditions using a torsion configuration. Detailed microstructural observations of specimens were performed before and after the experiments to identify the operative deformation mechanisms.

2. Experimental and analytical procedures

Our starting material was a natural lizardite–chrysotile serpentinite from Elba Island, Italy. The serpentinite occurs as veins consisting of lizardite and small amounts of chrysotile [12], and additional minerals (less than 1%). Lizardite grains of $0.3 \times 0.3 \times 0.9$ mm in average size are often embedded in a fibrous matrix of lizardite and some chrysotile (Fig. 1). Since the serpentinite has a weak shape preferred orientation, we cored the specimens from hand-size blocks parallel to the preferred orientation of (001) planes of serpentine.

All non-coaxial deformation experiments were performed at constant shear strain rates of 1×10^{-5} to 1×10^{-4} s^{-1}, confining pressures of 300 to 400 MPa and temperatures of 550 to 650 °C, using an internally heated Paterson gas-medium torsion apparatus (Table 1). In all experiments, confining pressure was first raised to 100 MPa; pressure and temperature were then increased simultaneously with a heating rate of 20 °C/min. A technical difficulty in our torsion experiments on serpentinite

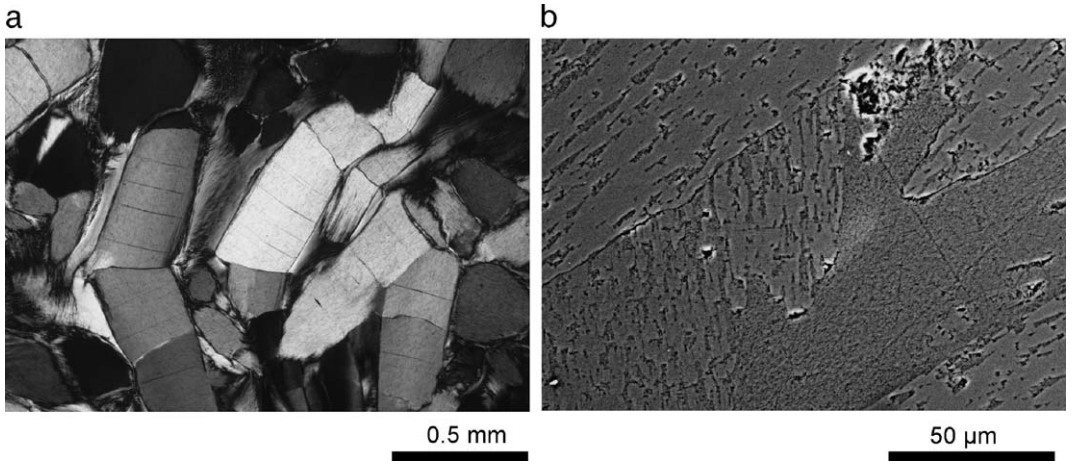

Fig. 1. Microstructures of the starting material. (a) Cross-polarized microphotograph showing elongate lizardite crystals embedded in a fibrous lizardite and chrysotile matrix. (b) Backscattered electron image. Different grey levels are due to surface relief from sample preparation.

Table 1
Experimental conditions and results of torsion experiments

Run number	Dimensions of deformed zone		Temp.	Confining pressure	Strain rate	Bulk shear strain	Local shear strain*	Total heating duration	Density		Reaction progress**
	Length (mm)	Diameter (mm)	(°C)	(MPa)	(1/s)	(–)	(–)	(hours)	Before (g/cm^3)	After (g/cm^3)	(%)
PO453	7.32	8.78	550	305	1E− 05	0.92	2.00	25.6	2.58	2.60	3.9
PO480	7.66	9.34	600	304	3E− 05	1.74	2.17	16.7	2.63	2.74	21.9
PO481	8.37	9.15	600	307	1E− 04	3.35	4.19	9.5	2.59	2.67	15.1
PO483	8.25	9.40	600	307	1E− 04	2.67	2.89	7.7	2.60	2.66	11.4
PO544	7.44	7.80	600	403	3E− 05	1.31	1.49	12.3	2.57	2.68	20.9
PO482***	9.08	11.83	650	305	–	–	–	5.2	2.57	2.75	33.8

Bulk shear strain was calculated from angular displacement and length of deformed part of specimen. Local shear strain was determined by measurement of the angle of a strain marker that was initially parallel to the axis of the sample column and rotated passively with increasing shear strain.

*In zone of localized deformation. Strain was measured from strain makers on copper jacket.

**Reaction progress was calculated assuming a linear relationship with density (see details in text).

***Static run.

was to prevent slip at specimen-piston interfaces. Even at elevated temperatures, serpentinite is strong and free fluid forming by the dehydration reaction migrates to the specimen-spacer interfaces, resulting in loss of friction there and preventing torsion deformation of the specimen. Therefore, we prepared specimens with a dog-bone shape and a central hole along their axial direction (Fig. 2). For a given torque (below the torque causing slip at the interface), the dog-bone shape allowed higher shear stresses to be attained in the part of the specimen where the diameter was smaller. The central hole acted as a fluid conduit, enabling easy escape for any fluid released during the dehydration reaction. The hole did not collapse and remained its shape during experiments, unless there was a large offset (>1 mm) along faults formed by shear localization. Specimens were placed between porous alumina spacers of 3 mm in thickness, which were connected to the atmosphere through pore pressure lines. Thus, our experiments were performed under drained conditions. Specimen diameter was ~ 9.2 mm in the central part and ~ 12 mm in the top and bottom parts. Deformation always occurred only in the part with the smallest diameter. Specimen length was ~ 20 mm. Specimens were jacketed with three copper sleeves of ~ 0.7 mm in total thickness and then put into a copper tube of ~ 0.25 mm in thickness with alumina and zirconia spacers.

A copper cylinder from the same source was deformed at the same temperatures and strain rates to calibrate the jacket strength. The results were consistent with the flow law for copper [13]. Therefore we used a simplified formulation of the flow law to correct the mechanical data for the effect of the strength of the copper jackets. The resolution of the internal torque cell is 0.2 Nm, corresponding to a shear stress of 1.3 MPa for 9.2 mm diameter specimens (assuming a stress exponent of $n=3$ for the calculation of shear stress from measured torque [14]). The temperature variation over the whole specimen was no more than 2 °C.

At the experimental pressure and temperature conditions, the serpentinite progressively transformed to olivine, talc, and H_2O. The reaction caused gradual changes in the density and porosity of the assemblage, resulting in overall variations of specimen dimensions. Axial dilation of the specimen generated friction between splines of the column end-piece and the internal load cell and

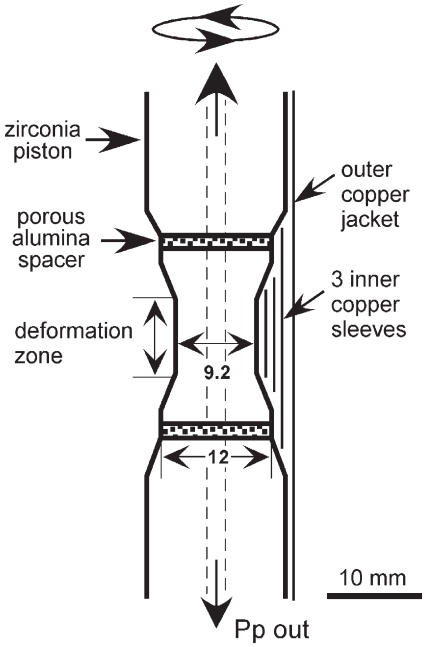

Fig. 2. Schematic diagram of sample assembly. Effective draining of pore fluid was achieved by a central hole through the specimen and porous alumina spacers placed at top and bottom of the specimen, allowing fluids to escape the system.

could be detected by the measurement of a small axial load (Fig. 3c). The duration of the axial dilation is defined as the period when the axial load increases

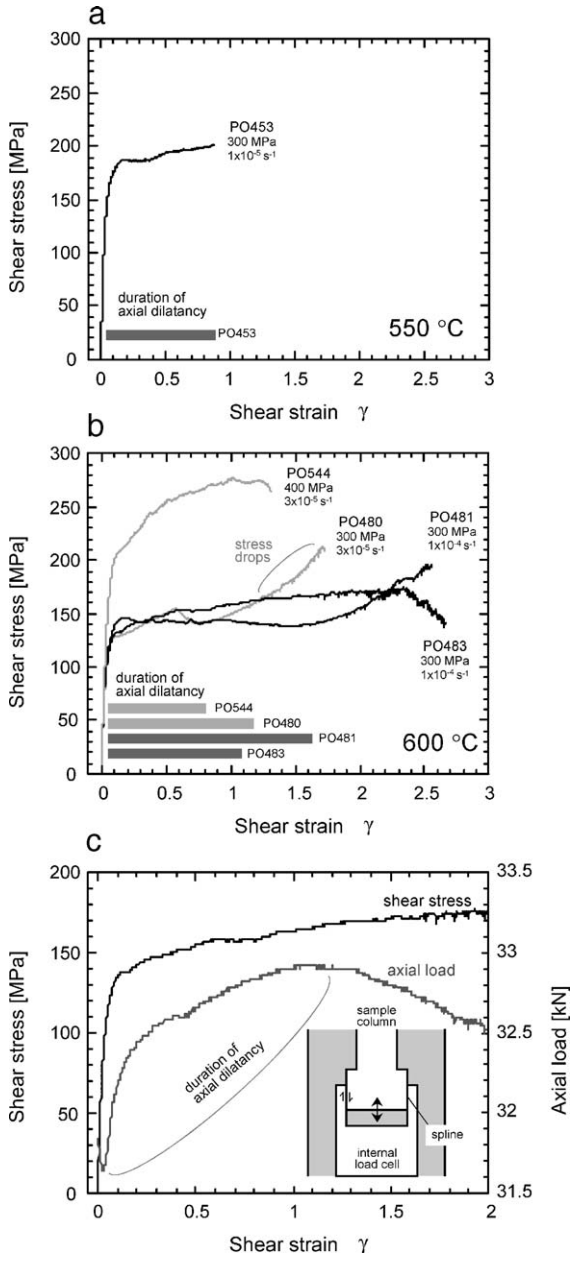

Fig. 3. Shear stress as a function of shear strain, plotted together with the duration of axial dilatancy of specimens deformed at 550 °C (a) and 600 °C (b). Stress drops of a few MPa typically occur during or at a late stage of strain hardening. Specimen PO481 was deformed to a total shear strain of 3.35, but mechanical data was lost after a shear strain of 2.5 due to loss of signal from the internal torque cell. (c) Shear stress and axial load as a function of shear strain (from PO483). Axial dilation of the sample causes friction between splines in the bottom part of the sample column (see inlet schematic diagram), leading to a transient increase in axial load from 0.03 to 1 in shear strain.

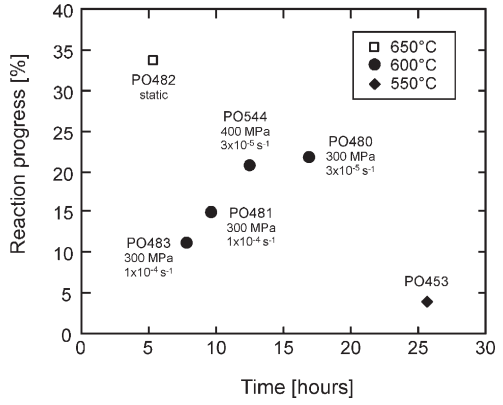

Fig. 4. Reaction progress as a function of time as calculated from density changes in the specimens.

transiently (Fig. 3). In all experiments, normal stresses due to specimen dilation (<15 MPa) are an order of magnitude smaller than measured shear stresses. Thus, the existence of a normal stress component does not significantly affect the general shape of the stress–strain curves.

After the experiments, deformed specimens were impregnated by epoxy several times during the polishing process and thin-sectioned close to the rim of the specimen and parallel to the cylindrical axis. In order to identify the reacted phases and to determine the deformation mechanisms governing the mechanical behaviour, the specimens were studied with X-ray diffractometry (XRD), electron probe micro-analysis (EPMA), optical microscopy, and scanning and transmission electron microscopy (SEM and TEM, respectively). Specimen densities were measured before and after the experiments using a helium pycnometer to estimate the reaction progress.

The reaction progress was calculated assuming a Fe-free system (9 serpentinite → 6 forsterite + 1 talc + 5 water) and a linear relationship with density. As serpentinite incorporates very little Fe, a Fe-free system is an appropriate approximation of the reaction. Densities ρ of 2570 kg/m^3 for serpentinite, 3270 kg/m^3 for forsterite, 2750 kg/m^3 for talc and 3089 kg/m^3 for 6 forsterite plus 1 talc [15] were used to calculate the reaction progress $100\times(\rho_{\text{after}}-\rho_{\text{before}})/(3089-2570)$, where ρ_{before} and ρ_{after} are the densities before and after the experiment, respectively.

3. Experimental results

Fig. 3 shows shear stress/shear strain curves, along with the duration of axial dilation of the specimens. All experiments show a similar mechanical behavior. Yielding

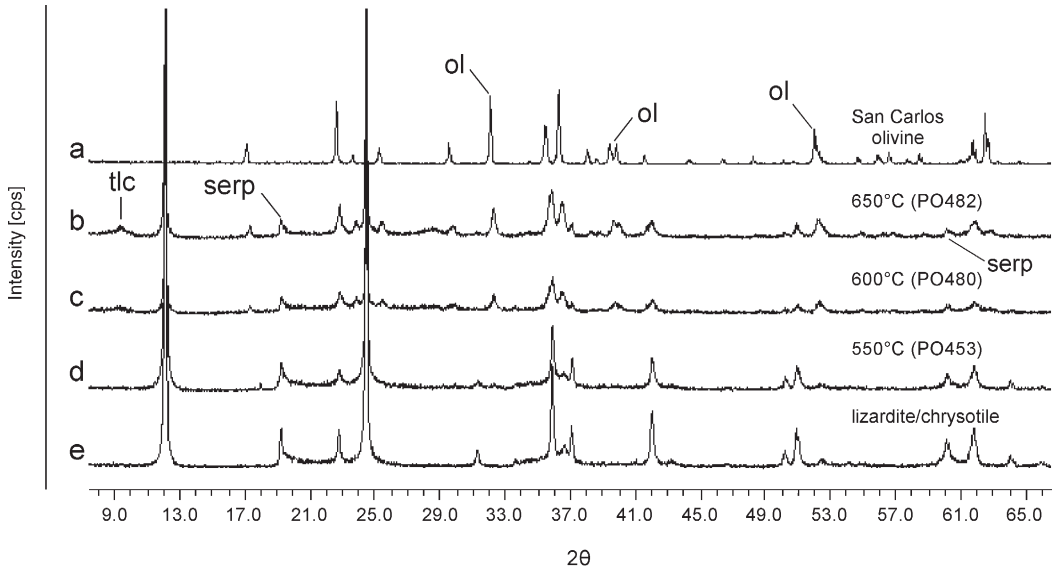

Fig. 5. Comparison of X-ray diffraction charts for San Carlos olivine (a), deformed specimens (b–d) and starting serpentinite (e). Arrows show the representative peaks of olivine (ol), serpentine (serp) and talc (tlc).

occurs at a shear strain of ~ 0.05 and is followed by a progressive increase in stress (strain-hardening stage) that starts concomitantly with dilatancy but continues even after dilatancy has stopped. The one exception is run PO481, which shows nearly steady state behavior after yielding up to a shear strain of ~ 2 before the hardening stage appears. The slope of the stress/strain curve becomes steeper after an acquired strain that is smaller at 3×10^{-5} s^{-1} (run PO480) than at the higher strain rate of 1×10^{-4} s^{-1} (runs PO481 and 483), suggesting that the increase in strain-hardening rate may be linked to reaction progress.

The yield stress shows a negative temperature dependence (~ 170 MPa at 550 °C and ~ 130 MPa at 600 °C, at 300 MPa in confining pressure). An increase in the confining pressure from 300 to 400 MPa at 600 °C results in an increase in the yield stress from ~ 130 MPa to ~ 190 MPa, representing a positive pressure dependence typically observed in the brittle field.

A large number of small stress drops (a few MPa) typically observed during strain hardening may be due to multiple slip along microfractures during fault formation (see Section 4). After the peak shear stress (~ 270 MPa and ~ 170 MPa in runs PO483 and PO544, respectively), strain weakening corresponds to the formation of a visible fault at ~ 30° to the axis of maximum principal stress (σ_1).

The reaction progress as a function of time is shown in Fig. 4. The top 5 mm of each specimen, where no deformation took place, were used for density measurements. As microstructural observations indicate that the reaction is enhanced by deformation (i.e. in the undeformed parts of the sample reaction takes place only along grain boundaries, whereas in deformed parts the reaction products are observed also within grains and typically along foliation planes), these estimates represent a lower limit for the actual reaction progress. Even though experimental conditions such as pressure and strain rate vary between experiments, the reaction progress always becomes larger as temperature and time increase. A thermocouple placed 3 mm above the sample central hole recorded frequent temperature perturbations, which were attributed to decompressing

Table 2
Representative chemical compositions of starting material and of specimen deformed at 550 °C

wt.%	Starting material		Deformed specimen		
			Clast	Matrix	
	Lizardite	Chrysotile		Dark phase	Bright phase
SiO_2	40.23	42.35	40.35	41.88	42.05
TiO	0.00	0.01	0.00	0.00	0.03
Al_2O_3	3.49	1.67	3.69	3.76	3.91
FeO[a]	4.08	2.70	3.92	4.04	4.23
MnO	0.02	0.03	0.05	0.06	0.04
MgO	38.50	37.54	39.23	40.16	41.13
CaO	0.00	0.05	0.01	0.01	0.00
NaO	0.00	0.00	0.04	0.01	0.00
Total	86.32	84.35	87.28	89.92	91.39

[a] Calculated assuming all of the iron in the ferous (2+) state.

H_2O escaping from the specimen during the dehydration reaction. Typically, the perturbations started as soon as the temperature reached 600 °C, implying that the onset of the reaction was immediate. A thermocouple within the furnace was used to control the temperature, and therefore the sample temperature remained quite stable during the experiments despite temperature perturbations recorded by the thermocouple placed above the sample.

The increase of reaction progress with temperature is confirmed by powder XRD data (Fig. 5). While chart *d* in Fig. 5 (PO453 deformed at 550 °C) does not show clear peaks of talc and olivine, serpentine peak intensities (e.g. $2\theta = 19.2$, 31.3, 60.1) decrease compared with those measured for the starting material (chart *e*). At temperatures above 550 °C talc ($2\theta = 9.4$) and olivine (e.g. $2\theta = 32$, 39.5) peaks are clearly visible (chart *c*) and their intensities become higher with increasing temperature (chart *b*).

The chemical composition of the samples also changes with temperature (Table 2). In the starting material, the compositions of lizardite and chrysotile (~ 86 and ~ 84 total wt.% of the oxides, respectively) indicate an H_2O content in the structure of about 15 wt.%, consistent with that found in the literature for this material [12]. The average total wt.% of the oxides increases during deformation at 550 °C, although there are great variations in grain to grain measurements. Undeformed lizardite grains behaving as clasts show relatively less total wt.% than well-deformed grains that form the foliation (Table 2; also see Section 4 below). Density, XRD and chemistry data all confirm that the dehydration reaction takes place progressively during deformation at the chosen experimental conditions.

4. Microstructures

Fig. 6 shows microstructures with different amounts of shear strain in specimens deformed at 600 °C. The original shape and size of lizardite grains are still preserved in the undeformed parts of the specimens (top part of the microphotographs), while in the deformed parts the grains become elongated and grain size

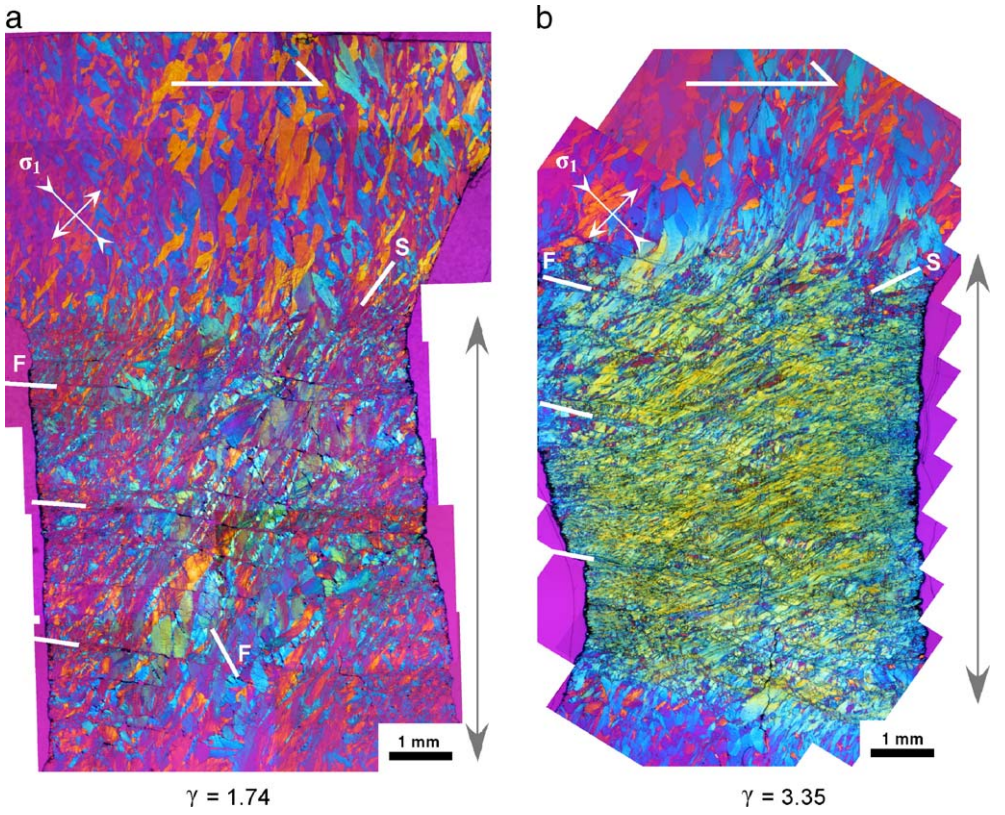

Fig. 6. Microphotographs of tangential sections under polarized microscope with inserted compensation plate showing widely distributed microfractures and strongly developed CPO in the deformed parts of the specimens. Right sense of shear. (a) Run PO480. (b) Run PO481. Dominant orientations of fractures (F) and S-foliations (S) are shown by thick lines. Vertical arrows show the deformed zones where the specimen diameter is smaller (cf. Fig. 2).

decreases with increasing shear strain. A foliation (S-plane) defined by elongated grains becomes visible (shape preferred orientation; SPO) and tilts progressively towards the shear direction with increasing shear strain. The development of a strong crystallographic preferred orientation (CPO) is documented by the preferred alignment of deformed grains resulting in a greenish color of the shear zone in Fig. 6b. Changes in crystallographic orientation are typically observed within sheared individual grains at the boundaries between deformed and undeformed zones, implying that the CPO developed by crystal plasticity.

Microfractures oriented at 30–35° to σ_1 are well developed and their number also increases with shear strain. Some of the microfractures have accommodated slip with displacements up to 80 μm. Their formation may correspond to small stress drops measured during the experiments. Crosscutting relationships between plastic and brittle features (highly sheared grains cut by microfractures) indicate that plastic and brittle processes occurred simultaneously during the deformation.

Though reaction products are easily distinguished from original lizardite by color contrast with back-scattered electron imaging (BSE), it is hard to identify individual olivine and talc grains. Fig. 7a and b show clast-matrix and S–C structures in deformed specimens. Chemical analyses indicate that darker grey clasts are slightly dehydrated lizardite grains (see total wt.% in column 4 in Table 2), while the highly deformed lighter grey matrix is more dehydrated and contains both serpentine and reactant phases (columns 5 and 6 in Table 2). In many areas, elongated domains of reactants have developed in localized shear zones (Fig. 7c). Clearly, deformation is localized in regions where the reaction is most advanced. Pores (Fig. 7d) are not always observed in highly deformed zones (lighter grey; Fig. 7c) and seem to have collapsed by shearing in many domains. These ductile microstructures appear to result from crystal plastic deformation.

Intensely kinked lizardite grains are observed with the TEM (Fig. 8). The kinking involves delamination along and slip on the (001) planes of the serpentine. No direct observation of dislocations was possible in these complex microstructures, and it is unclear whether slip is accommodated by a conventional plasticity mechanism (the term slip is used here as a descriptive term without

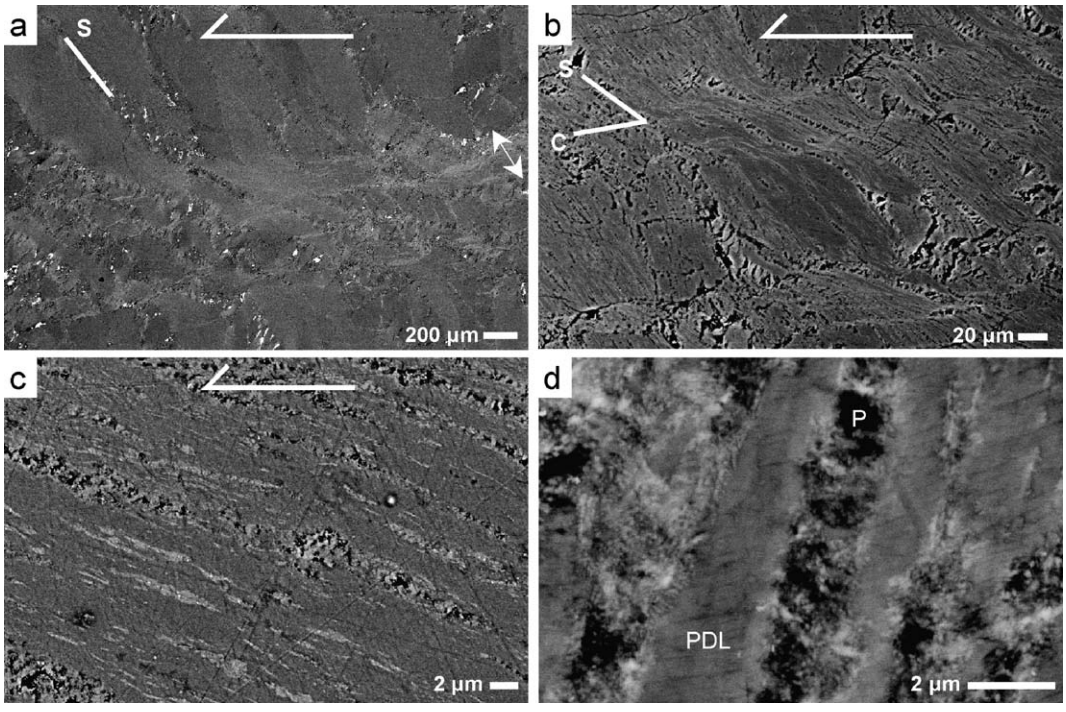

Fig. 7. Backscattered electron images of tangential sections of deformed specimens. Left sense of shear. (a) Clast-matrix structure in shear zone (Run PO453, T=550 °C, γ=0.92). Deformation is localized into a shear zone where the reaction is most advanced (white arrows). (b) Typical S–C structure (Run PO480, T=600 °C, γ=1.74). Black areas are pore space formed by the reaction. (c) Enlarged view of zone where deformation is localized (Run PO480, T=600 °C, γ=1.74). Note that pore space is hardly observed in well-sheared zones. (d) Enlarged view around pores in less deformed area (Run PO483, T=600 °C, γ=2.67). Pores are surrounded by brighter reacted phase. PDL: partially dehydrated lizardite, P: pore.

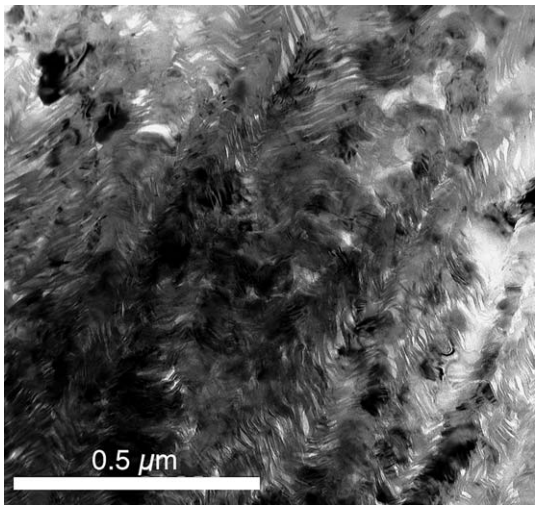

Fig. 8. TEM micrograph of deformed lizardite (Run PO483). Kinking, slip on (001) planes and the dehydration reaction produce considerable micro-porosity (small white areas) in the specimen. All the material in the image is lizardite. Some grains are in a different diffraction condition and appear dark in the image.

necessarily referring to dislocation glide mechanisms). However, the lattice of the lizardite is bent without detectable fractures so that crystal plastic deformation is likely. The bending causes considerable porosity on a small scale distributed pervasively throughout the deformed portion of the specimen. As deformation and dehydration reaction occur at the same time, the porosity development appears to produce an interconnected network of pores, increasing the permeability of the specimen. Thus, processes of deformation, porosity formation, and permeability increase occur simultaneously and may well be directly connected. In the region of the image, no olivine and talc are shown but talc is occasionally observed in other regions with the TEM.

5. Discussion

5.1. Semi-brittle deformation

In all experiments, large-strain deformation of serpentinite during dehydration produces features such as strong CPO and S–C structures that are typical for plastic processes. TEM observations indicate intense bending of and slip on (001) planes, consistent with plastic rotation of the serpentine crystal structure. Shear localization is evident in areas that are more dehydrated. Thus, as the dehydration reaction and deformation likely take place simultaneously in lizardite grains. The CPO results from slip and rotation of (001) planes in partially dehydrated serpentinite, possibly assisted by the release of fluid during the dehydration.

In addition to plastic features, microstructures show widespread arrays of fractures and micro-faults. Grain size reduction during deformation is mainly due to phase transformation and cataclastic processes rather than dynamic recrystallization. Brittle and plastic processes are clearly simultaneously active. Dilatancy occurs during plastic deformation (Fig. 8) and the relationship between pore pressure and plastic deformation is yet unclear. The positive dependence of strength on confining pressure and observed microstructures are consistent with deformation being in the semi-brittle field. In addition, the strain hardening indicates that no geometric weakening has occurred despite the rotation of the dominant slip plane (001) of serpentine towards the shear plane during CPO development.

5.2. Strain hardening mechanisms

Here we suggest three possible mechanisms responsible for the strain hardening behavior of serpentinite observed during dehydration.

(1) *Increase in effective pressure due to fluid drainage*: The serpentine dehydration reaction to olivine, talc and H_2O at our experimental conditions results in a reduction of solid volume, producing pore space of 26 vol.% and fluid of 44 vol.% with respect to an initial volume of serpentine. Thus, excess pore fluid pressures inevitably occur inside the specimen even under drained conditions, because the initial permeability of serpentinite is quite low. Specimen dilatancy due to microcracking during deformation lowers the high pore fluid pressure as fluid escapes from the specimen interior, increasing the effective pressure and resulting in strain hardening. The evidence for this process is found in experiments PO480 and PO481, where the shear stress increases substantially at the end of the dilatancy period (Fig. 3b), i.e. when drainage becomes more efficient than pore pressure build-up and hardening occurs as a consequence of increasing effective pressure. In addition to the effect of dilatancy, the dehydration reaction itself may enhance the strain hardening behavior by forming an interconnected porosity (Figs. 7d and 8). The rapid development of such an interconnected pore network may increase the permeability by as much as three orders of magnitude [10]. Similar processes of pore pressure change were observed during the dehydration of gypsum [16,17].

(2) *Compaction hardening*: As mentioned above, the reaction yields at least 26% porosity when the reaction is fully completed. Such a pore space must progressively be compacted due to the confining pressure and the differential stress. For instance, the reaction progress estimated from undeformed parts of specimens in Table 1 indicates that the porosity has evolved from almost 0% to ~ 4–5% after deformation at 600 °C. Considering that the reaction is enhanced in deformed parts of the specimens, the actual pore space in deformed serpentinite may be even larger (e.g., the porosity estimated by image analysis in Fig. 7b is about 8%, while measurement of the reaction progress in Fig. 4 yields only 1% porosity). Static runs at 650 °C (PO482) show progressive axial shortening of the specimens. In deformed specimens, intensive compaction has occurred during or after the dilation period due to shear-enhanced compaction (see Fig. 7c). As reduction in porosity allows the rock to work harden (e.g., [18]), the compaction effect could in part explain the observed hardening behavior.

(3) *Formation of a stronger phase assemblage*: Complete dehydration of serpentinized rocks produces olivine rocks that are stronger when deforming by either cataclastic or plastic mechanisms [8]. Based on previous frictional experiments [19,20], the strength of serpentinites is expected to increase significantly with temperature, even though the serpentinite dehydration reaction yields not only a strong phase, olivine, but also 25 vol.% of a very weak hydrous phase, talc. Thus, formation of a mechanically stronger assemblage of reaction products as the reaction progresses may contribute to the strain hardening behavior. In this case, the hardening rate depends on the transformation rate of reactant phases.

We propose that the hardening behavior is due to the combination of these three effects. Since the reaction rate is enhanced at lower pore pressures, the decrease in pore pressure promotes the formation of both harder reaction product and additional reaction-induced pore space. Thus observed high hardening rates in later stages of the experiments (Fig. 3) may result from the progressive decrease in pore pressure, promoting all three hardening effects.

Under natural conditions, whether or not strain hardening occurs depends on the evolution of the pore pressure, which in turn is controlled by permeability evolution, compaction rate and reaction rate. At typical natural dehydration conditions for subducting slabs (i.e. pressure >3 GPa and temperature >620 °C) [6], serpentine transforms to olivine + enstatite + water [15]. This reaction results in a greater reduction in solid volume than the lower-pressure transformation and hence has the potential to enhance transient porosity. The reaction products, olivine and enstatite, are likely much stronger than the olivine and talc assemblage at lower pressure. Thus, the hardening behavior observed in our experiments could be even more pronounced during the higher-pressure transformation due to the formation of only mechanically strong phases, especially if fluids are effectively drained from subducting slabs and fluid pressure build-up is prevented.

The numerous small stress drops (Fig. 3) and shear localization in the reaction zone (Fig. 7a) observed in our experiments may be related to processes causing intermediate-depth earthquakes along subduction zones (e.g., [5,6]) and localization of deformation in natural shear zones [1,2] associated with serpentinite dehydration. Our experiments imply that the bulk strength of a serpentinized subducting slab increases during dehydration as fluid escapes from the slab, while local embrittlement and shear localization take place at sites where fluid pressure locally and transiently builds up.

6. Conclusions

Deformation of natural lizardite–chrysotile serpentinite to large shear strains (up to 3.3) under drained conditions during dehydration to olivine, talc and water produces shear localization, a strong CPO of partially dehydrated serpentine and widely distributed microfracturing. The evolving fabric of the specimens and the mechanical data indicate that deformation occurred in the semi-brittle field. The CPO is interpreted to have formed by slip and rotation of (001) planes in partially dehydrated serpentine. Brittle processes are enhanced by water through the increase in local pore pressure by release of fluid during the dehydration. Similarly, plastic deformation (bending and delamination of serpentine crystal structure) is probably also affected by local pore pressure. Continuous strain hardening is observed and may be explained by the combined effects of dilatancy related hardening, compaction hardening, and the formation of a stronger assemblage of reaction products. Feedback processes related to pore pressure changes controlled by permeability evolution, compaction rate, and reaction rate during deformation must be considered to extrapolate these results to the rheology of serpentinite-bearing rocks during dehydration in subducting slabs (e.g., [21–23]).

Acknowledgements

We thank E. Reusser for microprobe analyses and P. Ulmer and M. Mellini for providing serpentinite samples and very useful comments and suggestions. We also thank R. van der Hilst and two anonymous reviewers for constructive comments which have improved the manuscript. This work was funded by the Swiss National Fonds (#2000-0666.16 and #2-77410-04) and the Japan Society for the Promotion of Science (#16000199). M.B. acknowledges additional funding by the European Social Fund while in Toulouse.

References

[1] E.H. Hoogerduijn Strating, R.L.M. Vissers, Dehydration-induced fracturing of eclogite-facies peridotites: implications for the mechanical behavior of subducting oceanic lithosphere, Tectonophysics 200 (1991) 187–198.
[2] J. Hermann, O. Muntener, M. Scambelluri, The importance of serpentinite mylonites for subduction and exhumation of oceanic crust, Tectonophysics 327 (2000) 225–238.
[3] C.B. Raleigh, M.S. Paterson, Experimental deformation of serpentinite and its tectonic implications, J. Geophys. Res. 70 (1965) 3965–3985.
[4] S.H. Kirby, Intraslab earthquakes and phase changes in subducting lithosphere, U.S. Natl. Rep. Int. Union Geod. Geophys. 1990–1994, Rev. Geophys. 33 (1995) 287–297.
[5] S.M. Peacock, Are the lower planes of double seismic zones caused by serpentine dehydration in subducting oceanic mantle? Geology 29 (2001) 299–302.
[6] T. Yamasaki, T. Seno, Double seismic zone and dehydration embrittlement of the subducting slab, J. Geophys. Res. 108 (2003), doi:10.1029/2002JB001918.
[7] S.A.F. Murrell, I.A.H. Ismail, Effect of decomposition of hydrous minerals on mechanical properties of rocks at high pressures and temperatures, Tectonophysics 31 (1976) 207–258.
[8] K.H. Brodie, E.H. Rutter, The role of transiently fine-grained reaction-products in syntectonic metamorphism: natural and experimental examples, Can. J. Earth Sci. 24 (1987) 556–564.
[9] E.H. Rutter, K.H. Brodie, Experimental syntectonic dehydration of serpentinite under conditions of controlled pore water pressure, J. Geophys. Res. 93 (1988) 4907–4932.
[10] E. Tenthorey, S.F. Cox, Reaction-enhanced permeability during serpentinite dehydration, Geology 31 (2003) 921–924.
[11] H.Y. Jung, H.W. Green, L.F. Dobrzhinetskaya, Intermediate-depth earthquake faulting by dehydration embrittlement with negative volume change, Nature 428 (2004) 545–549.
[12] C. Viti, M. Mellini, Contrasting chemical compositions in associated lizardite and chrysotile in veins from Elba, Italy, Eur. J. Mineral. 9 (1997) 585–596.
[13] H.J. Frost, M.F. Ashby, Deformation-mechanism maps: the plasticity and creep of metals and ceramics, Oxford, Pergamon Press, New York, 1982, 166 pp.
[14] M.S. Paterson, D.L. Olgaard, Rock deformation tests to large shear strains in torsion, J. Struct. Geol. 22 (2000) 1341–1358.
[15] P. Ulmer, V. Trommsdorff, Phase relations of hydrous mantle subducting to 300 km, in: Y. Fei, C.M. Bertka, B.O. Mysen (Eds.), Mantle Petrology: field observations and high pressure experiments, The Geochemical Society, Special Publication, vol. 6, 1999, pp. 259–281.
[16] S.C. Ko, D.L. Olgaard, U. Briegel, The transition from weakening to strengthening in dehydrating gypsum: evolution of excess pore pressures, Geophys. Res. Lett. 22 (1995) 1009–1012.
[17] S.C. Ko, D.L. Olgaard, T.F. Wong, Generation and maintenance of pore pressure excess in a dehydrating system: 1. Experimental and microstructural observations, J. Geophys. Res. 102 (1997) 825–839.
[18] T.F. Wong, C. David, W.L. Zhu, The transition from brittle faulting to cataclastic flow in porous sandstones: mechanical deformation, J. Geophys. Res. 102 (1997) 3009–3025.
[19] D.E. Moore, R. Summers, J.D. Byerlee, The effects of sliding velocity on the frictional and physical properties of heated fault gouge, Pure Appl. Geophys. 124 (1986) 31–52.
[20] T. Shimamoto, The origin of large or great thrust-type earthquakes along subducting plate boundaries, Tectonophysics 119 (1985) 37–65.
[21] T.F. Wong, S.C. Ko, D.L. Olgaard, Generation and maintenance of pore pressure excess in a dehydrating system: 2. Theoretical analysis, J. Geophys. Res. 102 (1997) 841–852.
[22] V.N. Balashov, B.W.D. Yardley, Modeling metamorphic fluid flow with reaction-compaction-permeability feedbacks, Am. J. Sci. 298 (1998) 441–470.
[23] S.A. Miller, W. van der Zee, D.L. Olgaard, J.A.D. Connolly, A fluid-pressure feedback model of dehydration reactions: experiments, modelling, and application to subduction zones, Tectonophysics 370 (2003) 241–251.